

Total Variation Regularized Weighted Tensor Ring Decomposition for Missing Data Recovery in High-Dimensional Optical Remote Sensing Images

Minghua Wang¹, Student Member, IEEE, Qiang Wang², Member, IEEE, Jocelyn Chanussot³, Fellow, IEEE, and Danfeng Hong⁴, Member, IEEE

Abstract—Due to sensor malfunction and atmosphere disturbances, high-dimensional optical remote sensing (HORS) images often suffer from information missing, such as dead pixels and thick clouds. Tensor decomposition methods have been used to estimate the missing data of HORS images. However, most existing models hardly consider the inherent properties and effective structural information of HORS images. To this end, we propose a novel total variation (TV) regularized weighted tensor ring (TR) decomposition model to recover the missing content of HORS images. The TR decomposition has the powerful low-rank (LR) representation ability to recover the HORS data by employing three low-dimensional tensors, i.e., TR factors. An initialization step and proper weights are designed to enhance the flexibility for exploring different LR properties of TR factors. To further preserve the spatial smoothness, the local spatial TV from three directions is incorporated into the TR decomposition framework. Furthermore, an augmented Lagrange multiplier (ALM) algorithm is designed for solving the resulting optimization problem. Experiments on HORS images demonstrate the performances of the proposed method over the current state-of-the-art baselines.

Index Terms—Augmented Lagrange multiplier (ALM), high-dimensional optical remote sensing (HORS), low-rank (LR) property, tensor ring (TR) decomposition, total variation (TV) from three directions, TR factors initialization, weights.

I. INTRODUCTION

HIGH-DIMENSIONAL optical remote sensing (HORS) is one of the most promising techniques for capturing information about the Earth's surface. However, due to sensor failure and poor working conditions, HORS images, including hyperspectral data and multitemporal data sequence, often suffer from missing data problems, such as dead pixels and cloud cover [1]. This HORS image quality degradation hinders

the effectiveness of subsequent processing analysis, including feature extraction [2], land cover classification [3], spectral unmixing [4], and target detection [5].

Low-rank (LR)-based approaches have been widely applied to HORS image reconstruction. The LR matrix completion (LRMC) theory [6] was developed to solve the RS image recovery problems. Nevertheless, high-dimensional remote sensing (RS) images are emerged as a matrix by unfolding each dimension into a vector, which inevitably leads to the loss of high-dimensional inherent information. Naturally, RS images are represented as tensors and low-rank tensor completion (LRTC) has been successfully introduced into RS image recovery [7], [8]. Learning from high-accuracy LRTC (HaLRTC) [9], Ng *et al.* [10] first used tensor completion (TC) for recovering the missing data in HORS and studied an adaptive weighted TC (AWTC) method. Induced by the t-product, Lu *et al.* [11] defined a new tensor nuclear norm (TNN) and tensor-singular value decomposition (t-SVD). Based on the tensor theory, Wang *et al.* [12] and Srinidhuna and Baburaj [13] proposed new low-tuba-rank TC methods to estimate the missing values in HORS images. Zhao *et al.* [14] proposed a new tensor ring (TR) decomposition to represent a high-dimensional tensor by circular multilinear products on a sequence of third tensor. Yuan *et al.* [15] focused on the TR algorithm development and proposed a new model named tensor ring low-rank factors (TFLRF). However, the most recent works only exploit the LR prior information of RS images but neglect the local spatial smoothness constraints. Wang *et al.* [16] designed a global-local two-stream architecture for HORS image scene classification from the perspective of the multiscale representation. He *et al.* [17] combined the TR decomposition with the total variation (TV) operators along two spatial directions, but they directly utilized the original TR model [14], which may cause high sensitivity to rank selection [15]. To overcome these drawbacks, we propose a novel TV regularized weighted TR decomposition (TV-WTR) model. The main contributions of this letter can be summarized as follows.

- 1) We fuse a weighted TR decomposition and a TV from three directions (3DTV) into a unified framework for missing data reconstruction of HORS images. The TR decomposition is adopted to explore LR tensor information. The 3DTV regularization is used to capture the local spatial information more comprehensively.

Manuscript received January 8, 2021; revised March 16, 2021; accepted March 25, 2021. This work was supported in part by the National Natural Science Foundation of China under Grant 61876054. (Corresponding author: Minghua Wang.)

Minghua Wang and Qiang Wang are with the Department of Control Science and Engineering, Harbin Institute of Technology, Harbin 150001, China (e-mail: minghuawang1993@163.com; wangqiang@hit.edu.cn).

Jocelyn Chanussot is with Inria, CNRS, Grenoble INP, LJK, Université Grenoble Alpes, 38000 Grenoble, France, and also with the Chinese Academy of Sciences, Aerospace Information Research Institute, Beijing 100094, China (e-mail: jocelyn.chanussot@grenoble-inp.fr).

Danfeng Hong is with the Remote Sensing Technology Institute (IMF), German Aerospace Center (DLR), 82234 Wessling, Germany, and also with Signal Processing in Earth Observation (SiPEO), Technical University of Munich (TUM), 80333 Munich, Germany (e-mail: danfeng.hong@dlr.de).

Color versions of one or more figures in this letter are available at <https://doi.org/10.1109/LGRS.2021.3069895>.

Digital Object Identifier 10.1109/LGRS.2021.3069895

- 2) We analyze the latent LR spaces of three TR decomposition blocks to more properly exploit the LR property. According to the analysis, we design three LR tensors for the TR factor initialization and appropriate weights for different LR constraints on the TR spaces.

II. PROPOSED METHOD

For the reconstruction processing of an HORS image, \mathcal{T} , \mathcal{X} , and Ω denote the observed image, recovered image, and a binary tensor with 1 representing the observation location and 0 denoting the missing location, respectively. Fig. 1 shows tensor ring decomposition (TRD), which is to represent a high-order \mathcal{X} by multilinear products of a sequence of three-order tensors in circular form. According to the definition and Lemma [14], TRD can denoted as $\mathcal{X} = \Phi([\mathcal{G}]) = \Phi(\prod_{n=1}^N \mathcal{G}^{(n)})$, where $\mathcal{G}^{(n)} \in \mathbb{R}^{r_n \times I_n \times r_{n+1}}$, $n = 1, 2, \dots, N$, $r_0 = r_N$. The TRD-related optimization model can be given as follows:

$$\min_{\mathcal{X}, [\mathcal{G}]} \|\mathcal{X} - \Phi([\mathcal{G}])\|_F^2 \quad \text{s.t.} \quad \mathcal{X}_\Omega = \mathcal{T}_\Omega. \quad (1)$$

To enhance the robustness to rank selection of TRD, the low rankness of each TR factors is constrained and the TR LR factor (TRLRF) model is formulated as follows:

$$\min_{\mathcal{X}, [\mathcal{G}]} \sum_{n=1}^N \sum_{i=1}^3 \left\| \mathbf{G}_{(i)}^{(n)} \right\|_* + \frac{\lambda}{2} \|\mathcal{X} - \Phi([\mathcal{G}])\|_F^2 \quad \text{s.t.} \quad \mathcal{X}_\Omega = \mathcal{T}_\Omega. \quad (2)$$

Here, two types of tensor matricization/unfolding operations are employed in this letter. The first mode- n unfolding operator is denoted by $\text{unfold}(\mathcal{X}, n) = \mathbf{X}_{(n)} \in \mathbb{R}^{I_n \times I_1 \dots I_{n-1} I_{n+1} \dots I_N}$ [18]. Inversely, $\text{fold}(\mathbf{X}_{(n)}, n)$ denotes the folding of the matrix into a tensor. Another operator defined for TR [14] is represented as $\mathbf{X}_{\langle n \rangle} \in \mathbb{R}^{I_n \times I_{n+1} \dots I_N I_1 \dots I_{n-1}}$.

As shown in Fig. 1, we explore two types of prior, including the LR properties of TRD and the spatial smoothness of 3DTV. We measure the LR properties in the different TR factors $\mathcal{G}^{(n)}$ by using the distribution of the singular values. The correlations along mode-2 are much stronger than those along the other modes. This inspires two modifications: TR factor initialization and different weights for different unfolding operators.

- 1) Random TR factors $\hat{\mathcal{G}}^{(n)}$ are generated by distribution $N \sim (0, 1)$ and then unfolded along mode-2. The singular values Σ of the mode-2 matrix $\hat{\mathbf{G}}_{(2)}^{(n)}$ are reduced by the shrinking operator, e.g., $[\mathbf{U}, \Sigma, \mathbf{V}] = \text{SVD}(\hat{\mathbf{G}}_{(2)}^{(n)})$, $\Sigma' = \Sigma - \Sigma(k)$, where k is much less than the size of the mode-2 matrix. The new initial TR factors $\mathcal{G}^{(n)}$ are redefined as $\text{fold}(\mathbf{U}\Sigma'\mathbf{V}^T, 2)$.
- 2) Proper weights $\{\alpha_i\}_{i=1}^3$ should be designed for distinguishing the contributions of different nuclear norms in the unfolding of the TR tensor factors. Simultaneously, the distributions of singular values of the unfoldings of the TR factors along mode-2 decay faster than those of the unfolding along mode-1. Therefore, we denote $\{\alpha_i\}_{i=1}^3$ as $[\theta_1, \theta_2, \theta_3] = [1, \theta, 1]/(2 + \theta)$ and only θ needs to be predetermined. The weighted

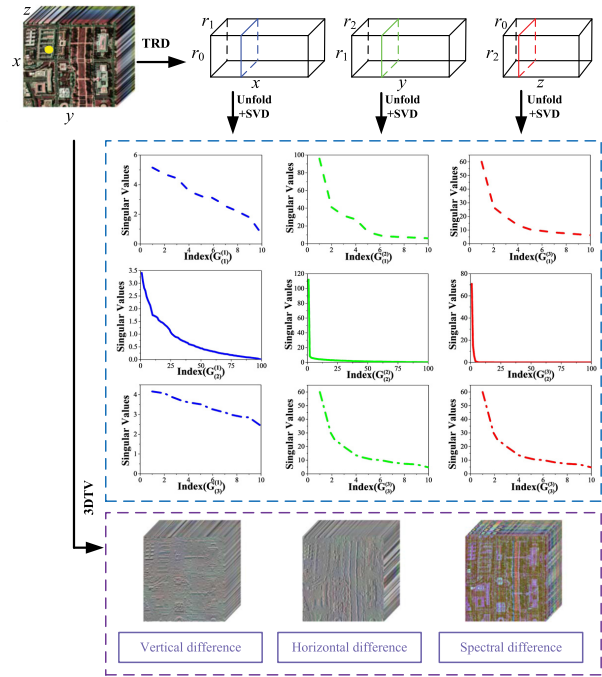


Fig. 1. Illustration of the proposed TV-WTR.

TR decomposition model can be calculated as

$$\min_{\mathcal{X}, [\mathcal{G}]} \sum_{n=1}^N \sum_{i=1}^3 \theta_i \left\| \mathbf{G}_{(i)}^{(n)} \right\|_* + \frac{\lambda}{2} \|\mathcal{X} - \Phi([\mathcal{G}])\|_F^2 \quad \text{s.t.} \quad \mathcal{X}_\Omega = \mathcal{T}_\Omega. \quad (3)$$

For an HORS image, exploring sufficient prior information is an important consideration. By combining the LR and smoothness structure properties together, we embedded the 3DTV regularization into the weighted TR decomposition model. The proposed TV-WTV model is formulated as

$$\min_{\mathcal{X}, [\mathcal{G}]} \sum_{n=1}^N \sum_{i=1}^3 \theta_i \left\| \mathbf{G}_{(i)}^{(n)} \right\|_* + \frac{\lambda}{2} \|\mathcal{X} - \Phi([\mathcal{G}])\|_F^2 + \tau \|\mathcal{X}\|_{3DTV} \quad \text{s.t.} \quad \mathcal{X}_\Omega = \mathcal{T}_\Omega \quad (4)$$

where the 3DTV term is defined as $\|\mathcal{X}\|_{3DTV} = \sum_{h,v,z} |\mathcal{X}_{h,v,z} - \mathcal{X}_{h-1,v,z}| + |\mathcal{X}_{h,v,z} - \mathcal{X}_{h,v-1,z}| + |\mathcal{X}_{h,v,z} - \mathcal{X}_{h,v,z-1}|$ with $\mathcal{X}_{h,v,z}$ the (h, v, z) th entry of \mathcal{X} .

To solve the problem (4), auxiliary variables $[\mathcal{M}] = \{\mathcal{M}^{(n,i)}\}_{n=1,i=1}^{N,3}$, \mathcal{W} and \mathcal{Z} are introduced and the equivalent minimization problem is rewritten as

$$\min_{\mathcal{X}, [\mathcal{G}], [\mathcal{M}], \mathcal{Z}} \sum_{n=1}^N \sum_{i=1}^3 \theta_i \left\| \mathbf{M}_{(i)}^{(n)} \right\|_* + \frac{\lambda}{2} \|\mathcal{X} - \Phi([\mathcal{G}])\|_F^2 + \tau \|\mathcal{Z}\|_1 \quad \text{s.t.} \quad \mathbf{M}_{(i)}^{(n)} = \mathbf{G}_{(i)}^{(n)}, \quad n = 1, 2, \dots, N, \quad i = 1, 2, 3 \\ \mathcal{W} = \mathcal{X}, \quad D(\mathcal{W}) = \mathcal{Z}, \quad \mathcal{X}_\Omega = \mathcal{T}_\Omega \quad (5)$$

where $D(\cdot) = [D_h(\cdot); D_v(\cdot); D_z(\cdot)]$ is the difference operator along three directions and D_h, D_v , and D_z are the first-order difference operators along different directions of HORS images. Based on the augmented Lagrange multiplier (ALM) algorithm, the abovementioned problem (5) is

transformed into the following augmented Lagrangian function and $\{\mathcal{Y}^{(n,i)}\}_{n=1,i=1}^{(N,3)}$, \mathcal{Y}_2 and \mathcal{Y}_3 are the Lagrange multipliers:

$$\begin{aligned} \min_{\mathcal{X}, [\mathcal{G}], [\mathcal{M}], \mathcal{Z}} & \sum_{n=1}^N \sum_{i=1}^3 \left(\theta_i \left\| \mathbf{M}_{(i)}^{(n)} \right\|_* + \langle \mathcal{Y}_1^{(n,i)}, \mathcal{M}_{(i)}^{(n,i)} - \mathcal{G}_{(i)}^{(n)} \rangle \right. \\ & \left. + \frac{\beta}{2} \left\| \mathcal{M}_{(i)}^{(n,i)} - \mathcal{G}_{(i)}^{(n)} \right\|^2 \right) \\ & + \frac{\lambda}{2} \|\mathcal{X} - \Phi([\mathcal{G}])\|_F^2 + \tau \|\mathcal{Z}\|_1 \\ & + \langle \mathcal{Y}_2, \mathcal{W} - \mathcal{X} \rangle + \frac{\beta}{2} \|\mathcal{W} - \mathcal{X}\|_F^2 \\ & + \langle \mathcal{Y}_3, D(\mathcal{W}) - \mathcal{Z} \rangle + \frac{\beta}{2} \|D(\mathcal{W}) - \mathcal{Z}\|_F^2 \\ \text{s.t. } & \mathcal{X}_\Omega = \mathcal{T}_\Omega. \end{aligned} \quad (6)$$

1) *Update $\mathcal{G}^{(n)}$* : All terms containing \mathcal{X} are extracted from the problem (6), and the $\mathcal{G}^{(n)}$ -related subproblem is obtained

$$\min_{[\mathcal{G}]} \sum_{n=1}^N \sum_{i=1}^3 \frac{\beta}{2} \left\| \mathcal{M}_{(i)}^{(n,i)} - \mathcal{G}_{(i)}^{(n)} + \frac{1}{\beta} \mathcal{Y}_1^{(n,i)} \right\|^2 + \frac{\lambda}{2} \|\mathcal{X} - \Phi([\mathcal{G}])\|_F^2. \quad (7)$$

The solution for this least-squares problem is

$$\begin{aligned} \mathcal{G}^{(n)} = \text{fold} & \left(\left(\sum_{i=1}^3 \left(\beta \mathbf{M}_{(2)}^{(n,i)} + \mathbf{Y}_{(2)}^{(n,i)} \right) + \lambda \mathbf{X}_{\langle n \rangle} \mathbf{G}_{\langle 2 \rangle}^{(\neq n)} \right) \right. \\ & \left. \times \left(\lambda \mathbf{G}_{\langle 2 \rangle}^{(\neq n),T} \mathbf{G}_{\langle 2 \rangle}^{(\neq n)} + 3\beta I \right)^{-1}, 2 \right). \end{aligned} \quad (8)$$

2) *Update $\mathcal{M}^{(n,i)}$* , by minimizing

$$\min_{[\mathcal{M}]} \sum_{n=1}^N \sum_{i=1}^3 \theta_i \left\| \mathbf{M}_{(i)}^{(n)} \right\|_* + \frac{\beta}{2} \left\| \mathcal{M}_{(i)}^{(n,i)} - \left(\mathcal{G}_{(i)}^{(n)} - \frac{1}{\beta} \mathcal{Y}_1^{(n,i)} \right) \right\|^2. \quad (9)$$

$\mathbf{M}_{(i)}^{(n)}$ is a nuclear norm model and has led to a closed form. By applying the shrinking operator $\mathbf{R}_{(\theta_i/\beta)}(\mathcal{G}_{(i)}^{(n)} - (1/\beta)\mathcal{Y}_1^{(n,i)}) = \text{diag}((\Sigma - (\theta_i/\beta)))$ to the singular value matrix Σ of $\text{SVD}(\text{unfold}(\mathcal{G}_{(i)}^{(n)} - (1/\beta)\mathcal{Y}_1^{(n,i)}), i) = [\mathbf{U}, \Sigma, \mathbf{V}]$, we obtain the estimated $\mathbf{M}_{(i)}^{(n)}$ and \mathcal{M}_k

$$\mathbf{M}_{(i)}^{(n)} = \mathbf{UR}_{\frac{\theta_i}{\beta}} \left(\mathcal{G}_{(i)}^{(n)} - \frac{1}{\beta} \mathcal{Y}_1^{(n,i)} \right) \mathbf{V}^T, \quad \mathcal{M}^{(n,i)} = \text{fold} \left(\mathbf{M}_{(i)}^{(n)}, i \right). \quad (10)$$

3) *Update \mathcal{W}* : Extract all \mathcal{W} -related items

$$\min_{\mathcal{Z}} \frac{\beta}{2} \left\| \mathcal{W} - \mathcal{X} + \frac{1}{\beta} \mathcal{Y}_2 \right\|_F^2 + \frac{\beta}{2} \left\| D(\mathcal{W}) - \mathcal{Z} + \frac{1}{\beta} \mathcal{Y}_3 \right\|_F^2 \quad (11)$$

and through a simple reduction, the linear system can be obtained

$$(\beta I + \beta D^* D) \mathcal{W} = \beta \mathcal{X} + \mathcal{Y}_2 + \beta D^*(\mathcal{Z}) - D^*(\mathcal{Y}_3) \quad (12)$$

where $D^*(\cdot)$ is the adjoint operator of D . Due to the block-circular structure of the operator D^*D , the subproblem (12) can be transformed into the Fourier domain

$$\mathcal{W} = \text{ifftn} \left(\frac{\text{fftn}(\beta \mathcal{X} + \mathcal{Y}_2 + \beta D^*(\mathcal{Z}) - D^*(\mathcal{Y}_3))}{(\beta + \beta Q)} \right) \quad (13)$$

Algorithm 1 TV-WTR

Input: Incomplete image \mathcal{T} , observation location Ω , TR rank r , parameters $k, \lambda, \theta_i, \beta$

- 1: **Initialization:** For $n = 1, 2, \dots, N$, random core tensors $\hat{\mathcal{G}}^{(n)}$ by distribution $N \sim (0, 1)$, the singular value decomposition of the mode-2 matrices $[\mathbf{U}, \Sigma, \mathbf{V}] = \text{SVD}(\hat{\mathbf{G}}_{(2)}^{(n)})$, new LR TR core tensors $\mathcal{G}^{(n)} = \text{fold}(\mathbf{U}(\Sigma - \Sigma(k))\mathbf{V}^T, 2)$, $\mathcal{M}^{(n,i)} = \mathcal{Y}_1^{(n,i)} = 0$, $\mathcal{Y}_2 = \mathcal{Y}_3 = 0$, $i = 0$, $\text{maxiter} = 300$, $\text{tol} = 1e^{-6}$.
- 2: **while** $0 \leq i \leq \text{maxiter}$ or $\|\mathcal{X} - \mathcal{X}_{\text{last}}\|_F^2 < \text{tol}$
- 3: $i = i + 1$;
- 4: $\mathcal{X}_{\text{last}} = \mathcal{X}$;
- 5: **update** core tensors $\{\mathcal{G}^{(n)}\}_{n=1}^N$ by (8);
- 6: $\mathcal{G}^{(n)} = \text{fold}((\sum_{i=1}^3 (\beta \mathbf{M}_{(2)}^{(n,i)} + \mathbf{Y}_{(2)}^{(n,i)}) + \lambda \mathbf{X}_{\langle n \rangle} \mathbf{G}_{\langle 2 \rangle}^{(\neq n)}) (\lambda \mathbf{G}_{\langle 2 \rangle}^{(\neq n),T} \mathbf{G}_{\langle 2 \rangle}^{(\neq n)} + 3\beta I)^{-1}, 2)$
- 7: **update** auxiliary variables $\{\mathcal{M}^{(n,i)}\}_{n=1,i=1}^{N,3}$ by (10);
- 8: $\mathbf{M}_{(i)}^{(n)} = \mathbf{UR}_{\frac{\theta_i}{\beta}}(\mathcal{G}_{(i)}^{(n)} - \frac{1}{\beta} \mathcal{Y}_1^{(n,i)}) \mathbf{V}^T$, $\mathcal{M}^{(n,i)} = \text{fold}(\mathbf{M}_{(i)}^{(n)}, i)$
- 9: **update** auxiliary variable \mathcal{W} by (13);
- 10: $\mathcal{W} = \text{ifftn}(\frac{\text{fftn}(\beta \mathcal{X} + \mathcal{Y}_2 + \beta D^*(\mathcal{Z}) - D^*(\mathcal{Y}_3))}{(\beta + \beta Q)})$
- 11: **update** auxiliary variable \mathcal{Z} by (15);
- 12: $\mathcal{Z} = \mathbf{S}_{\tau/(\beta)}[D(\mathcal{W}) + \frac{1}{\beta} \mathcal{Y}_3]$
- 13: **update** recovered tensor \mathcal{X} : $\mathcal{X} = \mathcal{T}_\Omega + \mathcal{X}'_{\bar{\Omega}}$, where $\mathcal{X}' = \text{ifftn}(\frac{\text{fftn}(\lambda \Phi(\mathcal{G}) + \beta \mathcal{Z} - \mathcal{Y}_2)}{(\lambda + \beta)})$
- 14: **update** the multipliers $\mathcal{Y}_1^{(n,i)} = \mathcal{Y}_1^{(n,i)} + \beta(\mathcal{M}^{(n,i)} - \mathcal{G}^{(n)})$
 $\mathcal{Y}_2 = \mathcal{Y}_2 + \beta(\mathcal{X} - \mathcal{W})$
 $\mathcal{Y}_3 = \mathcal{Y}_3 + \beta(D(\mathcal{W}) - \mathcal{Z})$
- 15: **end while**

Output: recovered image \mathcal{X} .

where $Q = |\text{fftn}(D_h)|^2 + |\text{fftn}(D_v)|^2 + |\text{fftn}(D_z)|^2$, and fftn and ifftn represent 3-D Fast Fourier transform and its inverse transform, respectively.

4) *Update \mathcal{Z}* : The \mathcal{Z} -related subproblem is rewritten as

$$\min_{\mathcal{Z}} \tau \|\mathcal{Z}\|_1 + \frac{\beta}{2} \left\| \mathcal{Z} - \left(D(\mathcal{W}) + \frac{1}{\beta} \mathcal{Y}_3 \right) \right\|_F^2. \quad (14)$$

This subproblem can be solved by soft-thresholding operator

$$\mathcal{Z} = \mathbf{S}_{\tau/(\beta)} \left[D(\mathcal{W}) + \frac{1}{\beta} \mathcal{Y}_3 \right] \quad (15)$$

where soft-thresholding operator $\mathbf{S}_\Delta(x)$ is defined as $\mathbf{S}_\Delta[x] = \text{sgn}(x) \cdot \max(|x| - \Delta, 0)$.

5) *Update \mathcal{X}* : The \mathcal{X} -related subproblem is a convex optimization with an extra equality constraint. \mathcal{X} is updated by the values of \mathcal{T}_Ω in the observation locations and by the values of $\mathcal{X}'_{\bar{\Omega}}$ in the estimation location, which is expressed as $\mathcal{X} = \mathcal{T}_\Omega + \mathcal{X}'_{\bar{\Omega}}$ where $\mathcal{X}' = \text{ifftn}(\text{fftn}(\lambda \Phi(\mathcal{G}) + \beta \mathcal{Z} - \mathcal{Y}_2)/(\lambda + \beta))$. The detailed procedure of TVWTR is presented in Algorithm 1.

III. EXPERIMENTAL RESULTS AND DISCUSSION

To evaluate the performance of the proposed model in HORS image reconstruction, we undertake two data experiments: the Washington DC Mall (WDC) data set and the

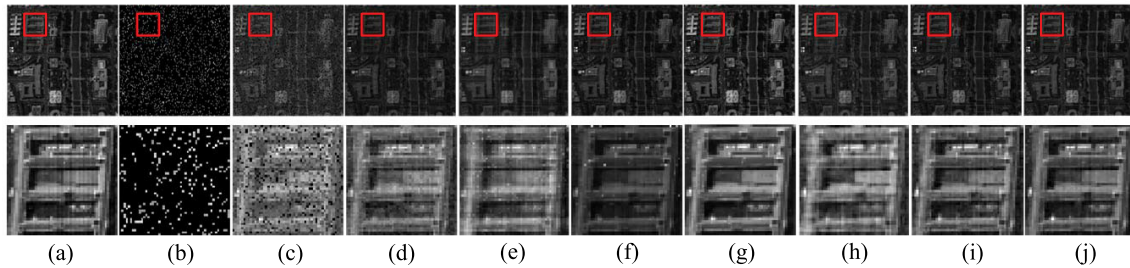


Fig. 2. Restoration results of different methods with 90% missing ratio. (a) Original band 1. (b) Missing. (c) LPMC. (d) LRTC. (e) HaLRTC. (f) STS-CNN. (g) WNSR. (h) TR. (i) TRLRF. (j) TVWTR.

TABLE I
QUANTITATIVE RESULTS OF ALL THE METHODS WITH
RANDOM MISSING AREA

Missing ratio	WDC Dataset									
	Index	Missing	LPMC	LRTC	HaLRTC	STS-CNN	WNSR	TR	TRLRF	TVWTR
0.5	MPSNR	17.19	46.96	48.94	49.81	51.53	53.80	53.41	<u>54.72</u>	56.90
	MSSIM	0.1478	0.9912	0.9935	0.9962	0.9980	0.9971	0.9982	<u>0.9985</u>	0.9990
	ERGAS	32.0847	1.2300	1.0905	0.9088	0.6436	0.5062	0.5315	<u>0.4524</u>	0.3630
	MSAD	44.9772	1.4342	1.1709	0.9992	0.7904	0.6184	0.6489	<u>0.5552</u>	0.4393
	MPSNR	15.73	37.48	43.26	42.31	49.38	48.78	47.38	<u>50.96</u>	53.39
0.7	MSSIM	0.0931	0.9633	0.9822	0.9803	0.9954	<u>0.9972</u>	0.9928	0.9968	0.9980
	ERGAS	37.9851	3.7354	1.9402	2.184	0.8292	0.8922	1.0414	<u>0.6924</u>	0.5322
	MSAD	56.8073	4.3818	2.1545	2.3436	1.0143	1.0842	1.2771	<u>0.8499</u>	0.6457
	MPSNR	14.64	24.66	35.41	31.72	40.28	41.02	40.32	<u>41.40</u>	43.34
	MSSIM	0.0447	0.5254	0.9192	0.8466	0.9713	<u>0.9833</u>	0.9658	0.9746	0.9842
0.9	ERGAS	43.063	13.5974	4.3617	6.8953	2.4213	2.2179	2.3971	<u>2.1065</u>	1.6813
	MSAD	71.5563	17.1278	4.9922	7.1969	2.9044	2.6555	2.8981	<u>2.5544</u>	2.0189

Sentinel-2 data set. We chose four metrics for evaluation: the mean peak signal-to-noise ratio (MPSNR), mean structural similarity index (MSSIM), the Erreur Relative Globale Adimensionnelle de Synthèse (ERGAS), and the mean spectral angle distance (MSAD).

1) *The WDC Data Set*: This data set is adopted and a subimage of size $256 \times 256 \times 30$ is selected with random missing data. We implement the following methods for comparison, i.e., LPMC [6], LRTC [12], HaLRTC [9], a spatial-temporal-spectral framework based on a deep convolutional neural network (STS-CNN) [19], weighted non-local second-order regularization (WNSR) [20], TR [14], and TRLRF [15]. Table I presents the quantitative evaluation results of recovery with the missing ratios 50%, 70%, and 90%. Due to the 3-D structure of HORS images destroyed, LPMC obtains the worst metric scores, especially when the missing ratio $r = 0.9$. LRTC achieves better evaluation results than those of HaLRTC in the case of 70% and 90%. This is mainly because, in the LRTC model, HORS images are regarded as 3-D tensors. STS-CNN and TR achieve similar performances when $r = 0.9$. WNSR produces better results than STS-CNN and TR and even obtains the second-best MSSIM values if $r = 0.7$ or 0.9. The performances of TRLRF and TVWTR remain stable even when the missing ratio is reaching 90%. Due to the considerations of the LR initiation and the TV regularization, the best performance is obtained from our TVWTR.

Fig. 2 shows the results of the WDC data set before and after recovery under $r = 0.9$. It is clear that LPMC fails to recover the HORS image. Although missing pixels disappear in the results of LRTC, HaLRTC, and TR, these methods produce more or fewer artifacts. STS-CNN, WNSR, and TRLRF perform better in reducing spectral distortion and show better performances. The proposed TVWTR method performs the best among all the compared algorithms. Due to exploiting the smoothing information, TVWTR preserves the

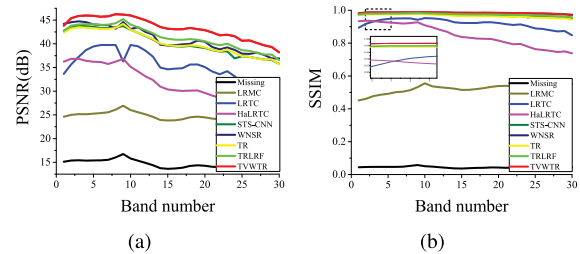


Fig. 3. PSNR and SSIM values of all bands with 90% missing ratio of WDC data. (a) PSNR. (b) SSIM.

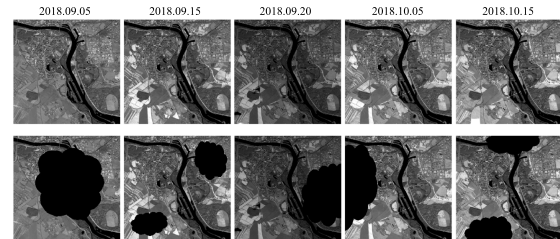


Fig. 4. Sentinel-2 multitemporal data sequence and different cloud coverings.

most details like sharp edges among all the methods. To further verify the recovery performance of the proposed method on each band, Fig. 3 shows the Peak signal-to-noise ratio (PSNR) and structural similarity index measure (SSIM) values of all bands with a 90% missing ratio of WDC data. The proposed TVWTR method achieves the highest metric scores in each band, which makes great consistency with the visual results.

2) *The Sentinel-2 Data Set*: We simulate the missing cloud coverings of time-series Sentinel-2 images and test the performances of different algorithms. As shown in the first row of Fig. 4, five time-series images (20-m spatial resolution, 10×10 km) were acquired by the Sentinel-2 sensor on September 5, 15, and 20, and October 5 and 15, 2018 from the Belgium area [21]. In the last row of Fig. 4, these HORS images were corrupted by various types of missing clouds. Due to LPMC invalid for removing the clouds, we dropped it for comparison. Table II gives a quantitative evaluation of the cloud removal experiment. WNSR and TRLRF achieve better MPSNR, ERGAS, and MSAD scores than pure TR, STS-CNN, and HaLRTC. Our TVWTR outperforms the other methods according to all the indices. Fig. 5 shows the visual results of removing clouds for Sentinel-2 data. The large region of the HORS image center is covered by the cloud. For HaLRTC, the large shadow still exists in Fig. 5(d). The marked areas with the red dotted circles display more or fewer artifacts

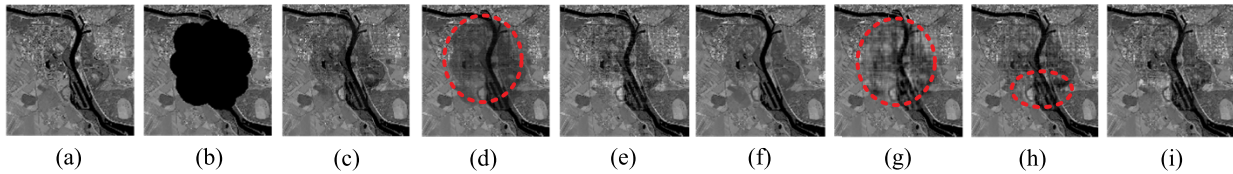


Fig. 5. Sentinel-2 image cloud removal results using different methods. (a) Original band 1. (b) Missing. (c) LRTC. (d) HaLRTC. (e) STS-CNN. (f) WNSR. (g) TR. (h) TRLRF. (i) TVWTR.

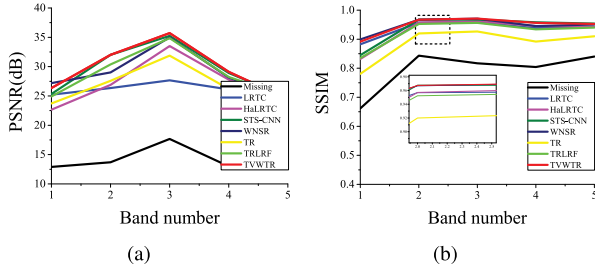


Fig. 6. PSNR and SSIM values of all bands with cloud removal of Sentinel-2 data. (a) PSNR. (b) SSIM.

TABLE II
QUANTITATIVE RESULTS OF ALL THE METHODS FOR
SENTINEL-2 CLOUD REMOVAL

Index	Missing	LRTC	HaLRTC	STS-CNN	WNSR	TR	TRLRF	TVWTR
MPSNR	14.14	25.74	26.96	28.08	28.74	26.97	28.64	29.53
MSSIM	0.7932	0.9356	0.9268	0.9348	<u>0.9365</u>	0.8857	0.9236	0.9435
ERGAS	32.7224	8.6183	8.3368	7.3715	<u>6.5997</u>	8.1620	6.8483	6.3575
MSAD	28.4891	6.9051	6.3952	5.8022	<u>5.2018</u>	6.6123	5.3881	4.9393

and texture discontinuity. WNSR produces the oversmoothing phenomenon in the central region. The proposed algorithm shows a satisfactory result without distortion. Fig. 6 shows the curves of PSNR and SSIM evaluation indices for each image. WNSR sometimes produces inaccurate PSNR scores, but it gets the second-best SSIM scores. HaLRTC has similar PSNR results with TRLRF. The proposed TVWTR outperforms the other compared methods in most bands.

IV. CONCLUSION

In this letter, we proposed a 3DTV regularization and weighted TR decomposition model to estimate the missing data of HORS images. By analyzing the LR properties of different TR factors, we design three LR tensors to initialize TR factors and three weights to constrain different nuclear norms of the TR factor unfoldings. The TV regularization is adopted to further characterize the smooth structure. The optimization problem is solved by the ALM framework. The experimental results verify the superior performance of the proposed method over the other compared algorithms.

REFERENCES

- [1] H. Shen *et al.*, "Missing information reconstruction of remote sensing data: A technical review," *IEEE Geosci. Remote Sens. Mag.*, vol. 3, no. 3, pp. 61–85, Sep. 2015.
- [2] B. Rasti *et al.*, "Feature extraction for hyperspectral imagery: The evolution from shallow to deep: Overview and toolbox," *IEEE Geosci. Remote Sens. Mag.*, vol. 8, no. 4, pp. 60–88, Dec. 2020.
- [3] D. Hong, L. Gao, J. Yao, B. Zhang, A. Plaza, and J. Chanussot, "Graph convolutional networks for hyperspectral image classification," *IEEE Trans. Geosci. Remote Sens.*, early access, Aug. 18, 2020 doi: 10.1109/TGRS.2020.3015157.
- [4] D. Hong, N. Yokoya, J. Chanussot, and X. X. Zhu, "An augmented linear mixing model to address spectral variability for hyperspectral unmixing," *IEEE Trans. Image Process.*, vol. 28, no. 4, pp. 1923–1938, Apr. 2019.
- [5] X. Wu, D. Hong, J. Chanussot, Y. Xu, R. Tao, and Y. Wang, "Fourier-based rotation-invariant feature boosting: An efficient framework for geospatial object detection," *IEEE Geosci. Remote Sens. Lett.*, vol. 17, no. 2, pp. 302–306, Feb. 2020.
- [6] J.-F. Cai, E. J. Candès, and Z. Shen, "A singular value thresholding algorithm for matrix completion," *SIAM J. Optim.*, vol. 20, no. 4, pp. 1956–1982, Jan. 2010.
- [7] M. Wang, Q. Wang, J. Chanussot, and D. Li, "Hyperspectral image mixed noise removal based on multidirectional low-rank modeling and spatial-spectral total variation," *IEEE Trans. Geosci. Remote Sens.*, vol. 59, no. 1, pp. 488–507, Jan. 2021.
- [8] F. Chen, P. Zhao, T. F. Tang, and Y. Zhou, "Fast low-rank decomposition model-based hyperspectral image classification method," *IEEE Geosci. Remote Sens. Lett.*, vol. 14, no. 2, pp. 169–173, Feb. 2017.
- [9] J. Liu, P. Musialski, P. Wonka, and J. Ye, "Tensor completion for estimating missing values in visual data," *IEEE Trans. Pattern Anal. Mach. Intell.*, vol. 35, no. 1, pp. 208–220, Jan. 2013.
- [10] M. K.-P. Ng, Q. Yuan, L. Yan, and J. Sun, "An adaptive weighted tensor completion method for the recovery of remote sensing images with missing data," *IEEE Trans. Geosci. Remote Sens.*, vol. 55, no. 6, pp. 3367–3381, Jun. 2017.
- [11] C. Lu, J. Feng, Y. Chen, W. Liu, Z. Lin, and S. Yan, "Tensor robust principal component analysis: Exact recovery of corrupted low-rank tensors via convex optimization," in *Proc. IEEE Conf. Comput. Vis. Pattern Recognit. (CVPR)*, Jun. 2016, pp. 5249–5257.
- [12] H. Wang, F. Zhang, J. Wang, and Y. Wang, "Estimating structural missing values via low-tubal-rank tensor completion," in *Proc. IEEE Int. Conf. Acoust. Speech Signal Process.*, May 2020, pp. 3297–3301.
- [13] M. Srinidhana and M. Baburaj, "Estimation of missing data in remote sensing images using t-SVD based tensor completion," in *Proc. Int. Conf. for Emerg. Technol. (INCET)*, Jun. 2020, pp. 1–5.
- [14] Q. Zhao, G. Zhou, S. Xie, L. Zhang, and A. Cichocki, "Tensor ring decomposition," 2016, *arXiv:1606.05535*. [Online]. Available: <http://arxiv.org/abs/1606.05535>
- [15] L. Yuan, C. Li, D. Mandic, J. Cao, and Q. Zhao, "Tensor ring decomposition with rank minimization on latent space: An efficient approach for tensor completion," in *Proc. AAAI Conf. Artif. Intell.*, vol. 33, Jul. 2019, pp. 9151–9158.
- [16] Q. Wang, W. Huang, Z. Xiong, and X. Li, "Looking closer at the scene: Multiscale representation learning for remote sensing image scene classification," *IEEE Trans. Neural Netw. Learn. Syst.*, early access, Dec. 17, 2020, doi: 10.1109/TNNLS.2020.3042276.
- [17] W. He, N. Yokoya, L. Yuan, and Q. Zhao, "Remote sensing image reconstruction using tensor ring completion and total variation," *IEEE Trans. Geosci. Remote Sens.*, vol. 57, no. 11, pp. 8998–9009, Nov. 2019.
- [18] T. G. Kolda and B. W. Bader, "Tensor decompositions and applications," *SIAM Rev.*, vol. 51, no. 3, pp. 455–500, Aug. 2009.
- [19] Q. Zhang, Q. Yuan, C. Zeng, X. Li, and Y. Wei, "Missing data reconstruction in remote sensing image with a unified spatial-temporal-spectral deep convolutional neural network," *IEEE Trans. Geosci. Remote Sens.*, vol. 56, no. 8, pp. 4274–4288, Aug. 2018.
- [20] J. Zheng, J. Jiang, H. Xu, Z. Liu, and F. Gao, "Manifold-based nonlocal second-order regularization for hyperspectral image inpainting," *IEEE J. Sel. Topics Appl. Earth Observ. Remote Sens.*, vol. 14, pp. 224–236, 2021.
- [21] Q. Zhang, Q. Yuan, J. Li, Z. Li, H. Shen, and L. Zhang, "Thick cloud and cloud shadow removal in multitemporal imagery using progressively spatio-temporal patch group deep learning," *ISPRS J. Photogramm. Remote Sens.*, vol. 162, pp. 148–160, Apr. 2020.